Supplement of Solid Earth, 17, 923–946, 2026
https://doi.org/10.5194/se-17-923-2026-supplement

Solid Earth
Open Access

Supplement of

Gas migration and slope instability in the Danube Fan: insights from integrated OBS-MCS seismic analysis

Helene-Sophie Hilbert et al.

Correspondence to: Helene-Sophie Hilbert (hhilbert@geomar.de)

Content:

- Text S1 – Wavefield rotation and vector consistency of OBS data
- Text S2 – Identification of converted S-wave phases
- Text S3 – Forward model assessment
- Figures S1 to S7 – OBS 3001 data examples for the processing flow and checking vector fidelity
- Figures S8 and S9 – Phase identification and PS conversion scheme
- Figures S10 to S13 – Forward model assessment
- Tables S1 and S2 – Seismic velocities, Vp/Vs-ratios, and pick uncertainties for the forward model layers

S1. Wavefield rotation and vector consistency of OBS data

S1.1 OBS instrument characteristics, data consistency and pre-processing

The OBS deployments included two instrument types (GEOMAR three-leg OBS and GEOMAR OBS-2002), both equipped with three-component geophones and hydrophones (Bialas and Flueh, 1999; Flueh and Bialas, 1996). The vertical and horizontal geophones were recorded with identical gain settings per instrument, ensuring consistent sensitivity across the three-component system. Hydrophone channels were recorded separately with instrument-specific response characteristics adapted to pressure measurements.

Although the two OBS designs differ in housing geometry and hydrophone type, all seismic recorders have a digital temperature-compensated crystal oscillator (DTCXO) with a 0.05 ppm accuracy over temperature as a time base. Time synchronisation is carried out before and after deployment using a GPS-based coded time signal generator. After the instrument recovery, the time drift is checked and compared with the original GPS units.

A standard pre-processing of the active source seismic data was performed following the GEOMAR standard procedures (Bialas et al., 2014). First, data processing was conducted with the manufacturer's software of the seismic recorders (SEND GmbH) to correct internal time slips, instrument response and other recording-related problems. The data were stored in PASSCAL format. Afterwards, single SEG-Y traces were generated by cutting the shots into traces with a defined time length based on the experimental geometry and shot interval. Further, a time offset of the trace and a reduction velocity were applied to determine the time of the first samples within a record. Thereby, the clock drift (skew) was corrected. The final SEG-Y format consists of a file header followed by the recorded traces for each shot.

S1.2 OBS relocation

During deployment, ocean-bottom seismometers may drift from their nominal drop positions due to water currents and uncertainties in ship navigation. Such offsets lead to asymmetric travel-time patterns in the record. These asymmetries introduce errors in the subsequent processing and modelling steps if not corrected for the actual location of the instrument.

Therefore, all OBS positions were relocated using first arrivals of the direct water wave, as described by Flueh and Grevemeyer (2005). The relocation procedure minimises the misfit between observed and calculated direct wave traveltimes by adjusting the receiver position relative to the known shot geometry and water velocity. Successful relocation is indicated by a symmetric and flattened direct wave arrival pattern within the receiver gathers (Fig. S1).

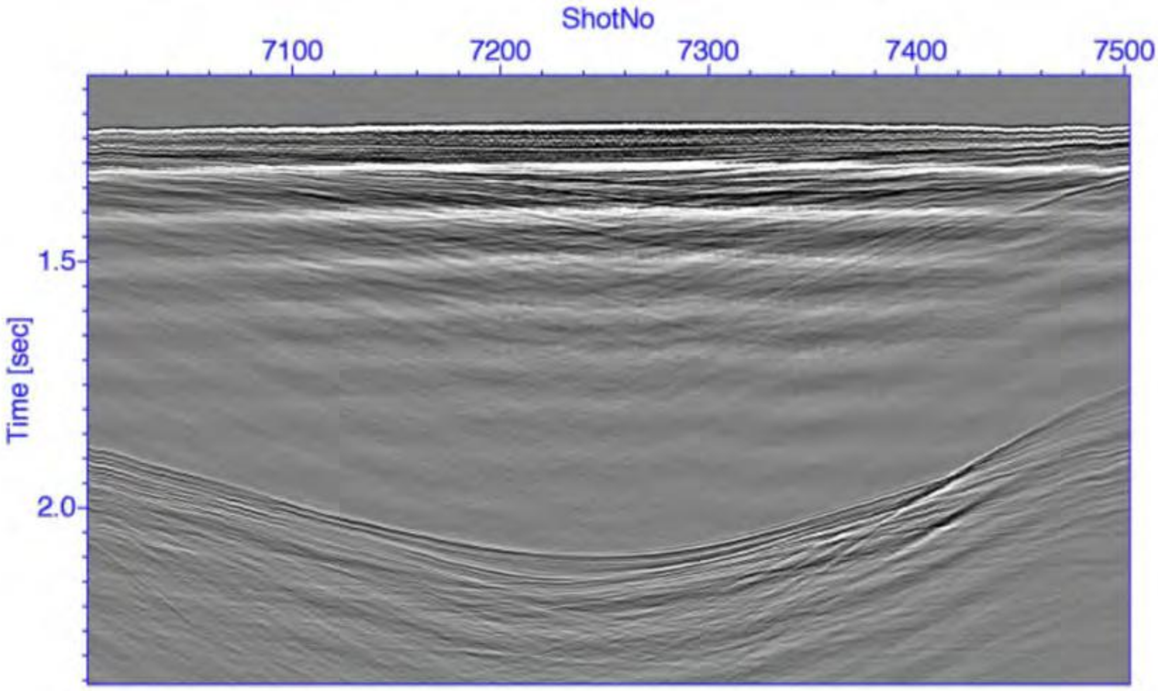

Figure S 1: Receiver gather for the OBS 3001 for midtrace 7252 - flattening of the direct wave after successful relocation.

Following relocation, additional static time corrections were applied where necessary to account for residual discrepancies between observed and calculated direct arrivals (Fig. S2). These corrections likely reflect a combination of navigation uncertainties, differences between bathymetric and seismic seafloor representations, and small uncertainties in the water velocities used during previous processing stages.

The consistency of the final geometry was verified using the traveltime difference Δt between the direct water wave t_d and its first multiple t_m. The difference is given by the geometry of the ray paths:

$$\Delta t = \frac{t_m - 3t_d}{2} \qquad (1)$$

Residual timing differences were small and within the estimated picking uncertainties, indicating that relocation and static corrections provided a reliable geometric framework for subsequent wavefield analysis and forward modelling.

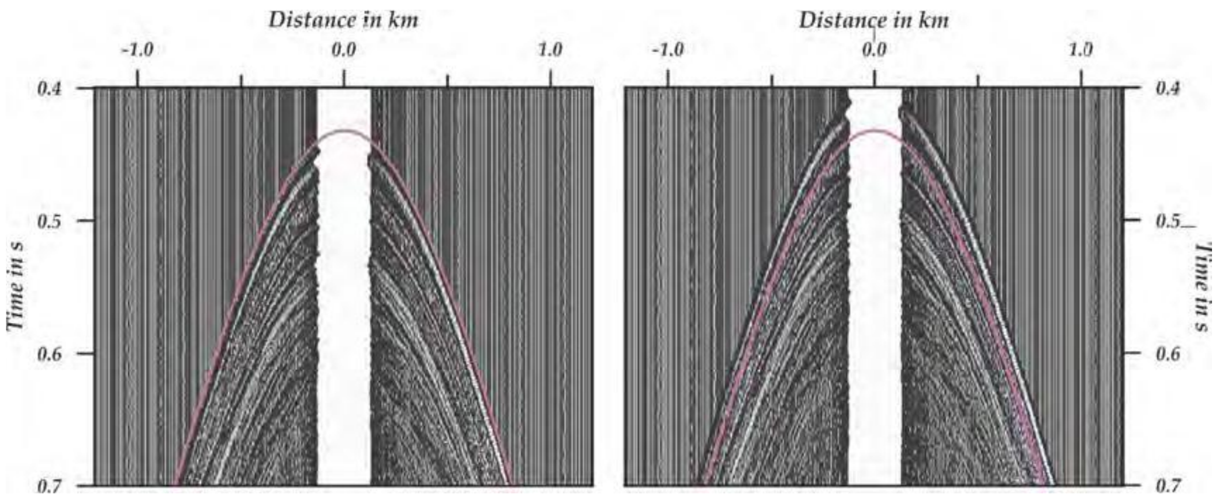

Figure S 2: Wiggle plot of OBS 3001. Pink line: theoretical direct wave. Left panel: Corrected signal delay after static time correction. Right panel: Data with signal delay before correction.

S1.3 Vector fidelity considerations

Rotation of the horizontal geophone components into radial and transverse directions implicitly assumes that the recorded wavefield can be treated as a vector quantity (Stein and Wysession, 2003; Yilmaz, 2001). This requires that the individual sensor components respond consistently to the same ground motion and that no significant relative gain or phase distortions exist between the horizontal channels.

Both OBS systems used during MSM-34 were equipped with identical three-component geophones with a natural frequency of 4.5 Hz (Bialas et al., 2014). The three orthogonal components were recorded simultaneously by the same acquisition system using identical processing chains. Standard GEOMAR pre-processing included corrections of recorder timing errors and instrument-specific response handling before conversion into SEG-Y format.

Although absolute sensor responses are not perfectly faithful representations of true ground motion, vector fidelity primarily depends on the relative consistency between the individual components rather than on absolute amplitude preservation (e.g., Havskov and Alguacil, 2016; Havskov and Ottemoller, 2010). If all components are affected similarly by the recording system, subsequent vector operations such as coordinate rotation remain valid as assumed by Maercklin (1999, 2001).

To evaluate potential component-dependent distortions, amplitude spectra of the horizontal and vertical geophone channels were compared over the frequency range relevant for the present study. The power densities were estimated using Welch's method (Welch, 1967), which reduces variance by averaging modified periodograms computed over overlapping windowed segments.

Here, we present the results of the analysis for OBS 3001 as an example (Fig. S3). Spectral comparison shows that the two horizontal geophone components exhibit very similar frequency characteristics over the dominant frequency signal band. Both components display comparable spectral shapes and amplitudes, including a common spectral break near the natural sensor frequency of 4.5 Hz. Below this frequency, spectral amplitudes increase consistently with the instrumental response of the geophone to a value of 1.

In contrast, the vertical component differs from the horizontal channels by generally higher spectral amplitudes. Such differences are expected because the components record different particle-motion directions and are affected differently by source radiation, seafloor coupling, incidence angle and sediment response (Duennebier and Sutton, 1995; Essing et al., 2021; Shearer and Orcutt, 1987).

After rotation, seismic energy becomes concentrated on the radial component, whereas the transverse component constains substantially lower amplitudes and mainly residual energy.

Spectral ratio analysis confirms this behaviour (Fig. S4). The X/Y ratios remain within the same order of magnitude over most of the frequency range, indicating comparable instrument responses of the horizontal channels. Following rotation, energy is preferentially concentrated on the radial component, whereas the transverse component exhibits substantially lower spectral amplitudes. This behaviour is consistent with predominantly radial particle motion generated by the airgun source and indicates that the rotation primarily redistributes physical wavefield energy rather than introducing artefacts.

Based on instrument design, standard pre-processing procedures, spectral consistency, and the physical plausibility of the rotated wavefield, the OBS recordings are considered sufficiently vector-consistent for the rotation and subsequent identification of the converted S-wave phases.

S1.4 OBS rotation and rotation angle estimation

The determination of the horizontal component rotation angle for each OBS is based on maximising the coherency of the recorded particle motion in the horizontal plane (Stein and Wysession, 2003; Yilmaz, 2001). This procedure assumes that a physically meaningful wavefield arrival (here: direct water-wave energy) exhibits a dominant linear polarisation that can be aligned into a single horizontal direction through rotation.

To ensure robustness, the analysis is restricted to carefully selected time windows around the direct arrival and applies identical preprocessing to both horizontal channels before any rotational testing. A bandpass filter is applied to isolate the frequency band of the dominant signal energy, reducing the influence of low-frequency tilt and high-frequency noise (e.g., Duennebier and Sutton, 1995; Essing et al., 2021; Shearer and Orcutt, 1987).

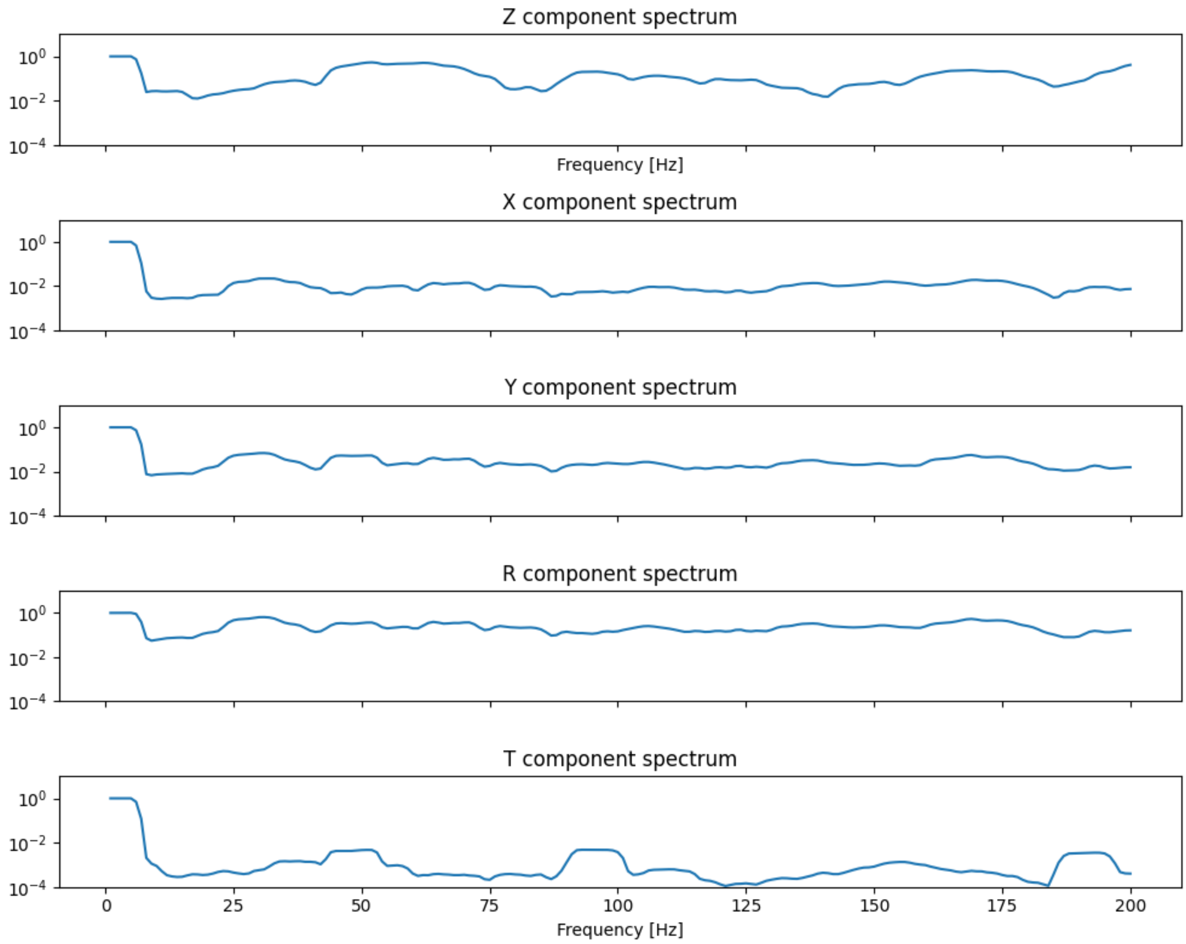

Figure S 3: Normalised power spectral density of the vertical (Z), horizontal (X, Y), radial (R), and transverse (T) components of OBS 3001. Spectra were calculated using Welch's method (Welch, 1967) and normalised to the maximum value of each component.

The data are extracted from the Seismic Unix (Stockwell, 1999) processing chain, where each component is treated consistently and stored in a unified 3-component structure. This ensures that subsequent rotation operates on co-registered time series with identical sampling and filtering history. Before rotation, a consistency check of the signal geometry is performed using hodograms in XY, ZX and ZY space (Fig. S5) to verify that the selected time window contains coherent particle motion (Flinn, 1965; Vidale, 1986).

The rotation angle is then determined by a systematic angular sweep from 0° to 360°. For each tested angle, the horizontal components are rotated using a 2-D rotation operator. After rotation, the signal is decomposed again into the horizontal components and a scalar energy measure is computed. The optimal rotation angle is defined as the angle that maximises the signal energy of one horizontal component (here H1), corresponding to maximum alignment of particle motion along a single axis (Flinn, 1965; Vidale, 1986). This approach is equivalent to maximising the variance of the projected signal and is closely related to principal component analysis (PCA) applied to the horizontal covariance matrix (e.g.,Jurkevics, 1988).

As an independent verification, PCA is applied directly to the unrotated horizontal components. The principal eigenvector of the covariance matrix defines the dominant polarisation direction, which provides an independent estimate of the rotation angle. Agreement between the energy-based rotation and PCA-derived angle indicates stable and well-conditioned horizontal component behaviour (Fig. S6).

This workflow implicitly assumes high vector fidelity of the recorded horizontal channels, meaning that both components respond consistently to the same ground motion and differ primarily by geometric orientation rather than instrument-induced distortion. Under these conditions, rotation is mathematically valid and physically meaningful.

After applying the optimal rotation angle, the particle motion in the horizontal-radial system becomes highly coherent (Fig. S7). The RT and ZR components align closely and form an almost linear hodogram, indicating that the dominant energy is now consistently projected onto a single physically meaningful propagation direction. This is a strong indicator that the instrument orientation has been correctly resolved.

The ZT component, however, retains a slightly more complex pattern, forming an elliptical loop in the central part while still maintaining a clear preferred orientation ~45° offset from the dominant axis. This suggests that the vertical component still contains a mixture of wave types or residual coupling effects, which is expected in OBS data where conversions and 3-D wavefield complexity cannot be fully removed by rotation alone.

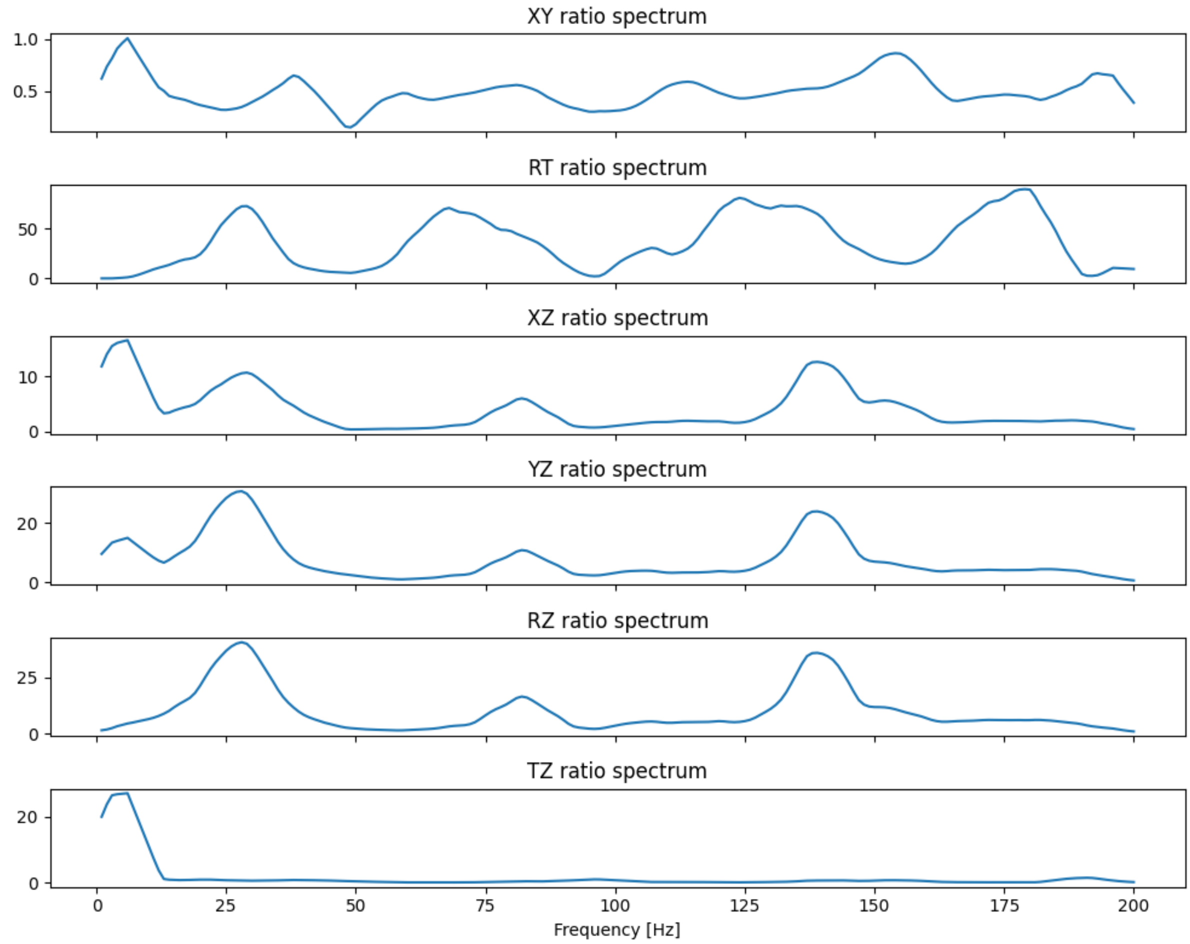

Figure S 4:Spectral amplitude ratios between vertical (Z), horizontal (X, Y), and rotated components (radial R and transverse T) for OBS 3001, computed from Welch power spectral densities (Welch, 1967). Ratios highlight the relative energy distribution between components across frequency. X/Y ratios remain close to unity, indicating similar horizontal instrument responses. Ratios involving Z reflect the higher vertical energy content and the expected sensor orientation sensitivity. After rotation, energy is strongly concentrated on the radial component (R/T) across most frequencies, while the transverse-to-vertical ratios remain low, consistent with predominantly radial particle motion and the absence of rotation-induced spectral distortions. A consistent spectral transition is observed near the natural sensor frequency (~4.5 Hz).

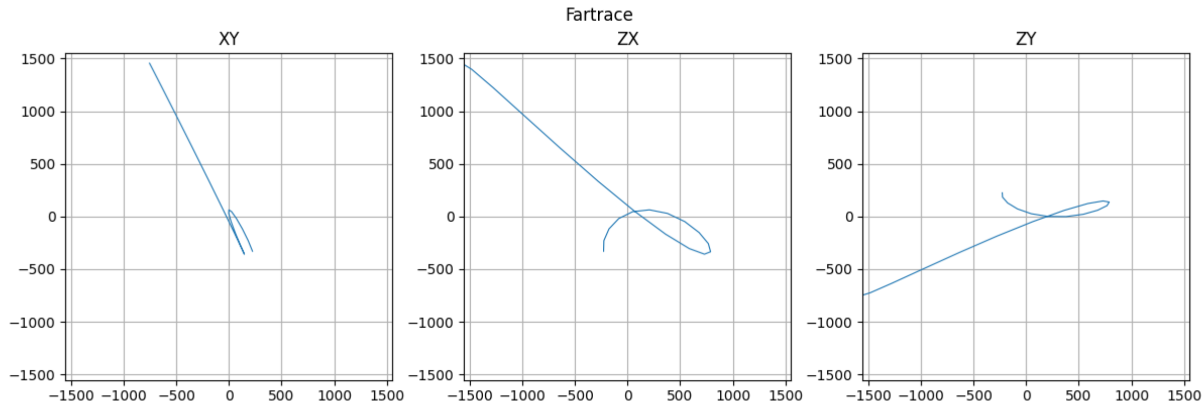

Figure S 5:Fartrace 7449 hodograms before rotation. Three-component particle motion is shown for the selected analysis window in XY, ZX, and ZY component space. The unrotated data exhibit a non-systematic distribution of particle motion, indicating a misalignment between the sensor axes and the true source-receiver geometry. The absence of a clearly linear polarisation axis reflects the arbitrary orientation of the horizontal OBS components prior to rotation and motivates the subsequent determination of an optimal rotation angle based on signal polarization.

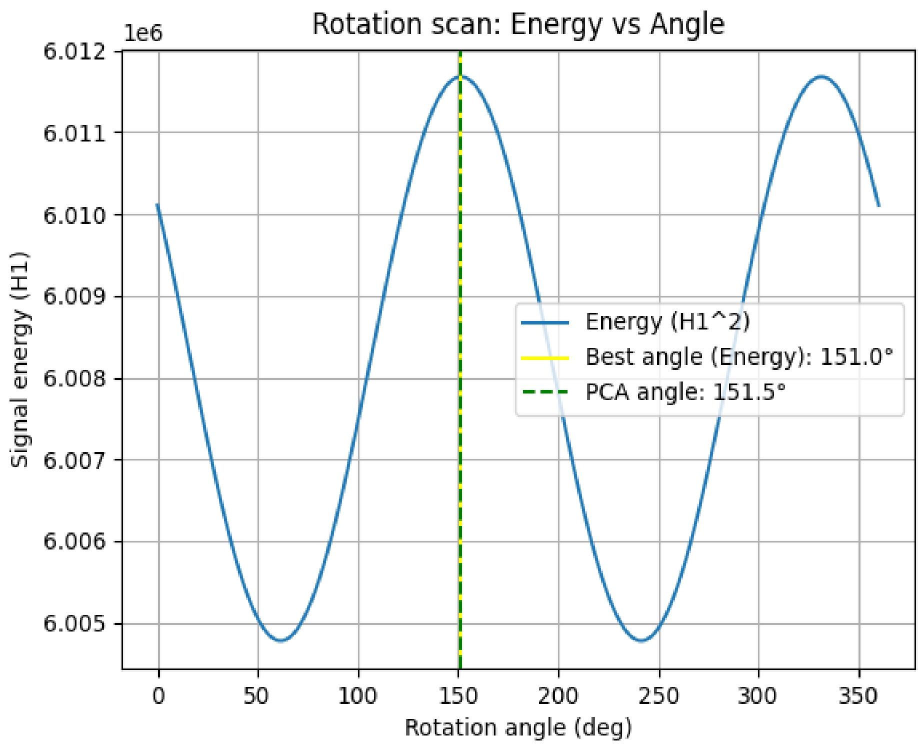

Figure S 6: Rotation scan of the horizontal components for determination of the optimal OBS rotation angle for station 3001. Signal energy (squared amplitude) of the H1 (Y) component is shown as a function of rotation angle (0°-360°). The optimal rotation angle is defined by the maximum of the H1 energy, corresponding to the strongest alignment of particle motion onto a single horizontal axis. For comparison, the PCA-derived orientation (green dashed line) and the energy-based optimum (yellow line) are indicated. Differences between both estimates reflect the distinction between variance-based (PCA) and signal-energy-based optimization approaches. In this case the uncertainty is 0.5°.

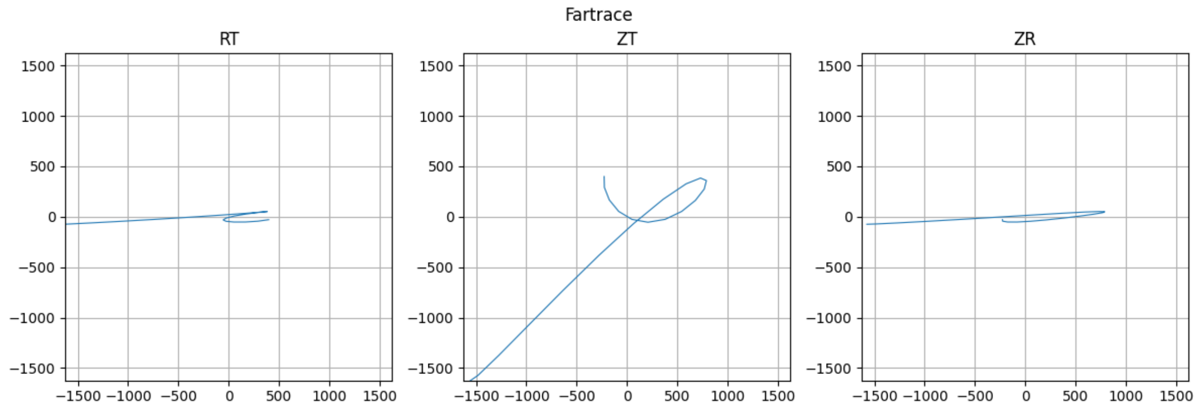

Figure S 7: Fartrace 7449 hodograms after rotation. Three-component particle motion is shown for the selected analysis window in RT, ZT, and ZR component space. The rotated data exhibit a nearly linear, co-aligned particle motion pattern, indicating successful alignment of the principal wavefield direction with the rotated coordinate system. In contrast, the ZT projection shows a more complex, slightly elliptical trajectory, while remaining largely linear and rotated by ~45° relative to the dominant RT-ZT direction. This behaviour reflects residual projection of mixed wavefield components, likely associated with converted or multiply polarised arrivals in the vertical-horizontal plane.

S2. Identification of converted S-wave phases

S2.1 Overview

The identification of converted shear-wave (PS) phases in ocean bottom seismometer (OBS) data is based on a combined structural and waveform-consistent interpretation workflow. The approach assumes that P-wave reflections and their corresponding converted S-wave phases originate from the same subsurface interfaces, consistent with standard PS conversion at impedance contrasts. Similar approaches to determine S-wave velocities have been successfully conducted in previous studies (e.g., Digranes et al., 1998; Eccles et al., 2009; Westbrook et al., 2008).

Rotated three-component data (Z, R, T) were used for phase analysis. The vertical or hydrophone component (Z/H) serves as the primary reference for P-wave reflection picking, while the radial component (R) is used for identification of corresponding converted S-wave energy.

S2.2 P-wave identification

As mentioned in the manuscript, P-wave reflections were manually picked on the hydrophone component (H) based on:

- waveform continuity across offset,
- lateral coherence between adjacent OBS stations,
- and structural guidance from multichannel seismic (MCS) reflection data.

MCS data were used as an external structural constraint to ensure lateral consistency of interpreted horizons and to reduce ambiguity in weak or overlapping arrivals (Fig. S8). Only laterally continuous reflection events with clear structural correspondence were used as P-wave reference phases.

S2.3 Identification of converted PS-waves

Converted S-wave phases were identified on the radial component by correlating interpreted P-wave reflection events with corresponding energy arrivals in the horizontal wavefield. The interpretation is based on the expected P-to-S conversion at subsurface interfaces (Fig. S9) and the resulting kinematic relationship between P and PS travel times.

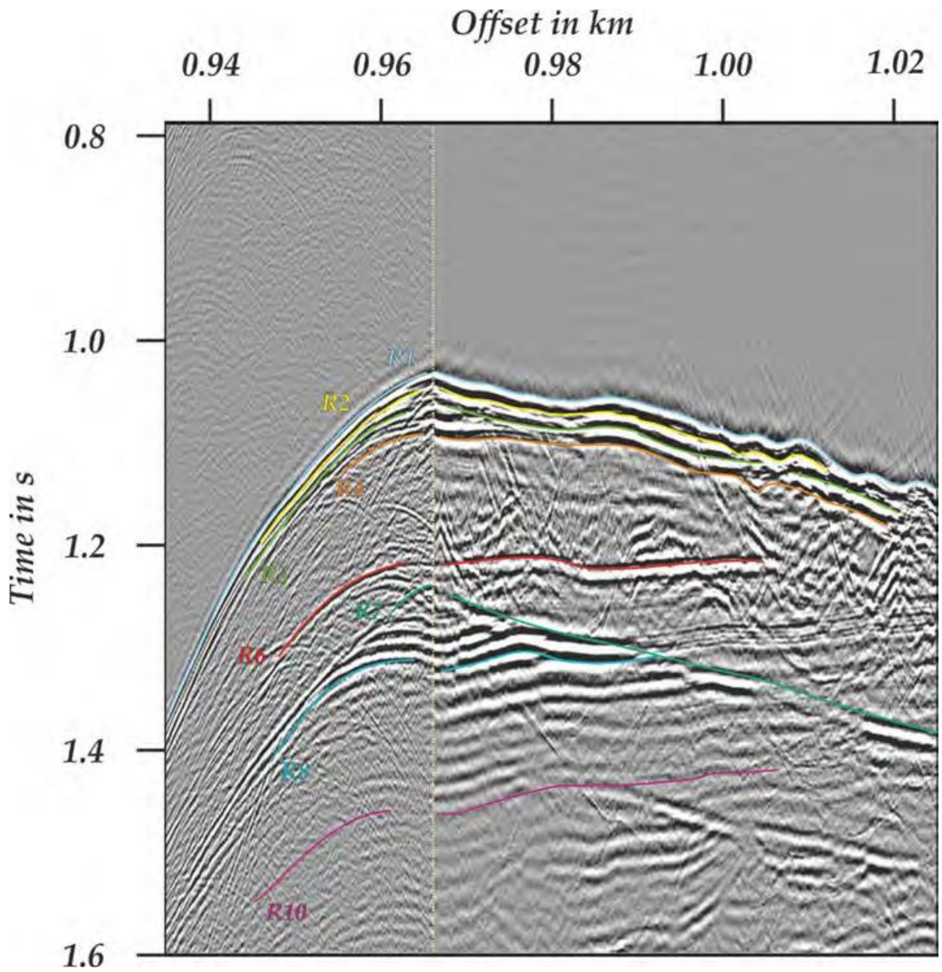

Figure S 8: Alignment of the OBH data with 2D MCS data. A Butterworth bandpass filter, bandpass filter (20 – 40 Hz) and equal amplitude scaling have been applied to the vertical component. Afterwards the data were adapted to the size and offset distance of the MCS data.

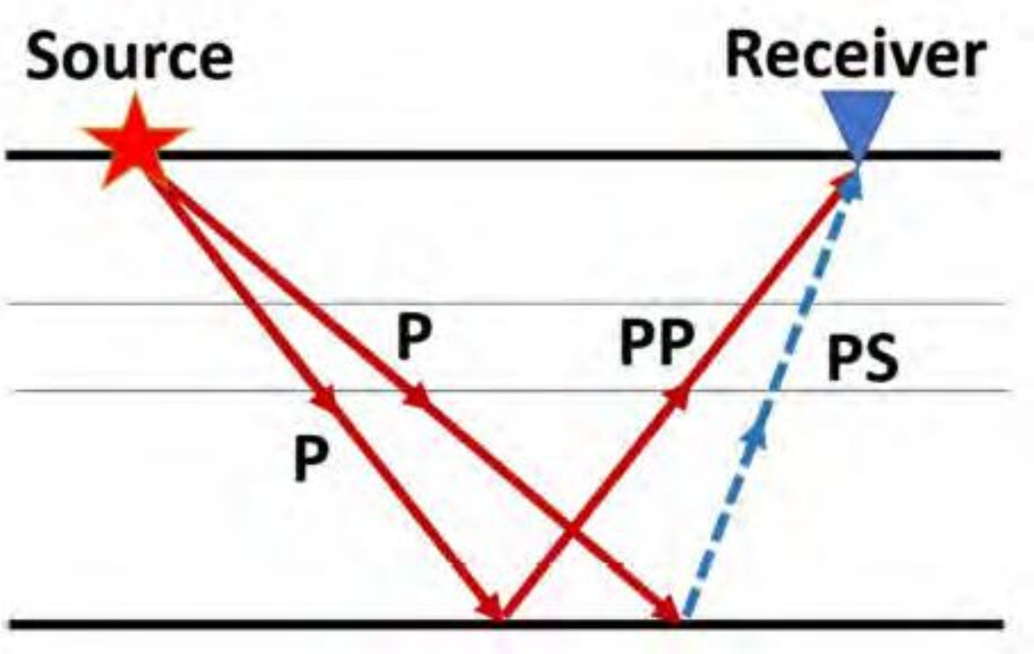

Figure S 9:Simplified scheme of P and PS conversion at the same interface. A downward propagating P-wave is converted into a PS-wave at the deepest point compared to a pure P-wave reflection. Note the shift of the reflection point toward the receiver.

Phase identification was guided by the following criteria:

1. Kinematic consistency: Candidate PS arrivals must exhibit a physically plausible moveout trend consistent with conversion at the interpreted reflector depth.
2. Waveform coherence: Identified phases must be traceable across multiple offsets and, where available, across neighbouring OBS stations.
3. Amplitude and polarisation behaviour: Converted phases are expected to show increased energy on the radial component relative to the transverse component after rotation into the source-receiver coordinate system.
4. Structural agreement: Phase picks must be consistent with reflector geometries derived from MCS data.

S2.4 Ambiguity handling and rejection criteria

Phase identification becomes increasingly ambiguous in the presence of overlapping arrivals, reduced signal-to-noise ratio at larger offsets, and complex wavefield interference. To ensure robustness, multiple candidate interpretations were evaluated. A phase was rejected if it:

- failed to reproduce consistent travel-time behaviour in forward modelling,
- lacked continuity across offsets or stations,
  or could not be associated with a structurally consistent reflector in MCS data.

Only phase interpretations that remained stable under these constraints were retained for velocity modelling.

S2.5 Vp/Vs constraints from reference models

To support physically consistent phase interpretation, typical Vp/Vs ratios from comparable marine sedimentary environments were considered as first-order constraints. Reference values were taken from published compilations for marine sediments and upper crustal materials (e.g., Hamilton, 1979), providing expected velocity ranges for unconsolidated to semi-lithified sediments.

These empirical constraints were used qualitatively to assess the plausibility of observed time differences between P-wave reflections and corresponding converted S-wave arrivals. In particular, they provided a reference range for expected S-wave delays relative to P-wave travel times at given reflector depths.

The Vp/Vs information was not implemented as a fixed inversion constraint but served as a consistency check during phase assignment and interpretation.

S2.6 Additional consistency constraints

To further improve the robustness of phase identification, the following criteria were applied:

- Multi-station consistency: Phase picks were required to be reproducible across adjacent OBS stations.
- Offset consistency: Converted phases had to exhibit systematic and physically plausible moveout behaviour with increasing source–receiver offset.
- Polarisation consistency: After rotation into the radial–transverse system, converted energy was expected to concentrate on the radial component, with minimal leakage onto the transverse component for purely compressional-to-shear conversions.
- Structural consistency: Phase picks were cross-validated against MCS reflection geometries to ensure compatibility with regional stratigraphy.

S2.7 Uncertainty considerations

Uncertainty in phase picking arises from waveform complexity, filtering effects, interference of overlapping arrivals, and finite sampling resolution. Following standard practice in OBS studies (e.g., Diehl, 2008), minimum timing uncertainty is constrained by the sampling interval (1 ms at 1000 Hz sampling rate). Additional uncertainty is introduced for low signal-to-noise arrivals and ambiguous onset definitions, increasing the actual picking uncertainty. Systematic uncertainty was further reduced by testing multiple window lengths and amplitude scalings to ensure stability of phase identification.

S2.8 Limitations

It is acknowledged that converted S-wave phase identification in wide-angle OBS data is inherently non-unique. In particular, interference between reflected phases, converted waves, and source-generated noise can lead to ambiguity in phase attribution.

Therefore, the presented phase set represents the most consistent solution under the combined constraints of waveform coherence, structural control, kinematic plausibility, and Vp/Vs-based physical reasoning rather than a uniquely determined classification.

S2.9 Summary

The identification of converted S-wave phases is based on an integrated interpretation framework combining:

- structural constraints from MCS data,
- waveform and polarisation analysis in rotated OBS coordinates,
- kinematic consistency across offsets and stations,
- and first-order Vp/Vs constraints from published reference models.

This multi-constraint approach ensures internally consistent phase assignments suitable for subsequent velocity modelling and Vp/Vs estimation.

S3. Forward model assessment

A first-order assessment of the forward model is typically obtained by a comparison between the observed and synthetic traveltimes derived from ray tracing and the ray coverage. In combination with statistical model parameters, such as the root-mean-square (RMS) misfit, this gives an estimation of the model quality. Figs. S10 and S11 display the observed and modelled traveltime picks and ray coverage of profile A for the P- and S-wave models, respectively. Similarly, Figs. S12 and S13 show the resulting comparison and ray coverage for the P- and S-wave model of profile B, respectively. In addition, the Tables S1 and S2 provide the modelled seismic P- and S-wave velocities, corresponding Vp/Vs-ratios, and pick uncertainties for each layer of both profiles.

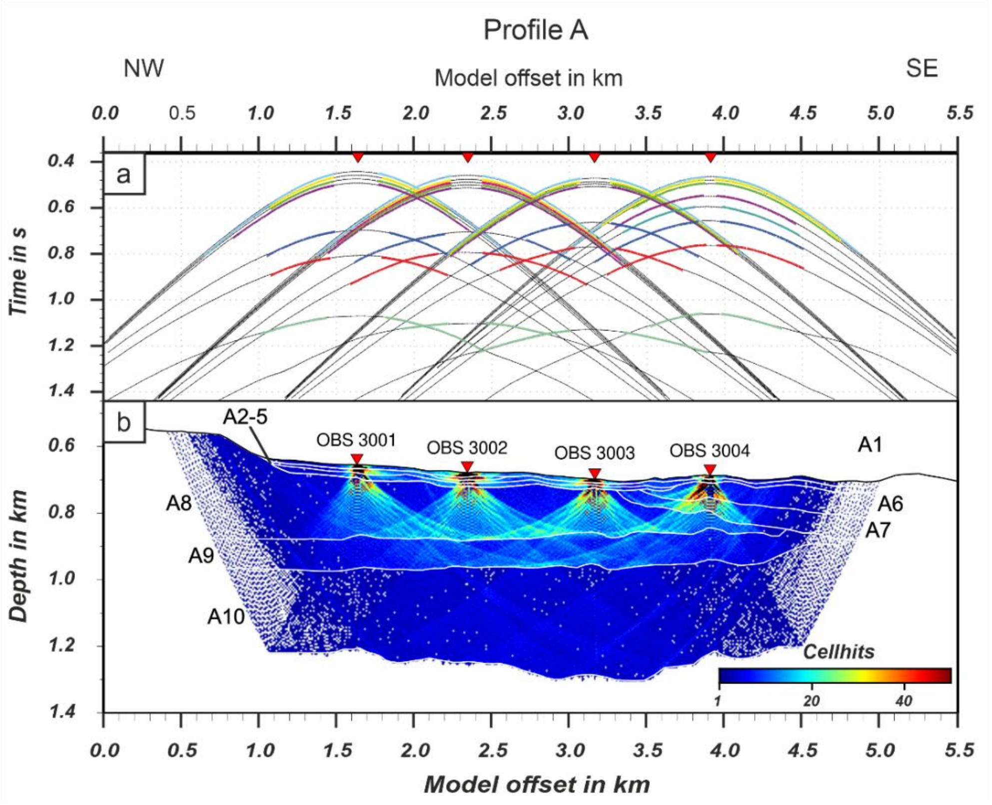

Figure S 10:Forward model assessment for the P-wave velocity model of profile A. (a) Comparison between the observed (coloured lines) and synthetic traveltime picks (black lines). (b) Ray coverage based on the ray density within the model cells.

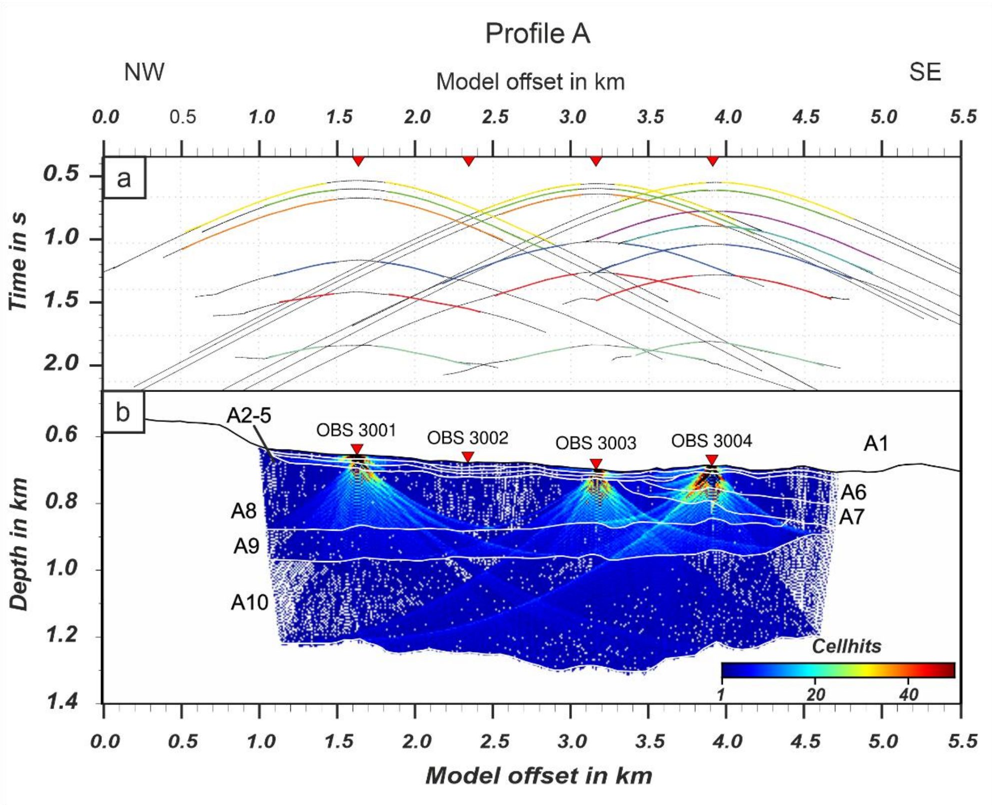

Figure S 11: Forward model assessment for the S-wave velocity model of profile A. (a) Comparison between the observed (coloured lines) and synthetic traveltime picks (black lines). (b) Ray coverage based on the ray density within the model cells.

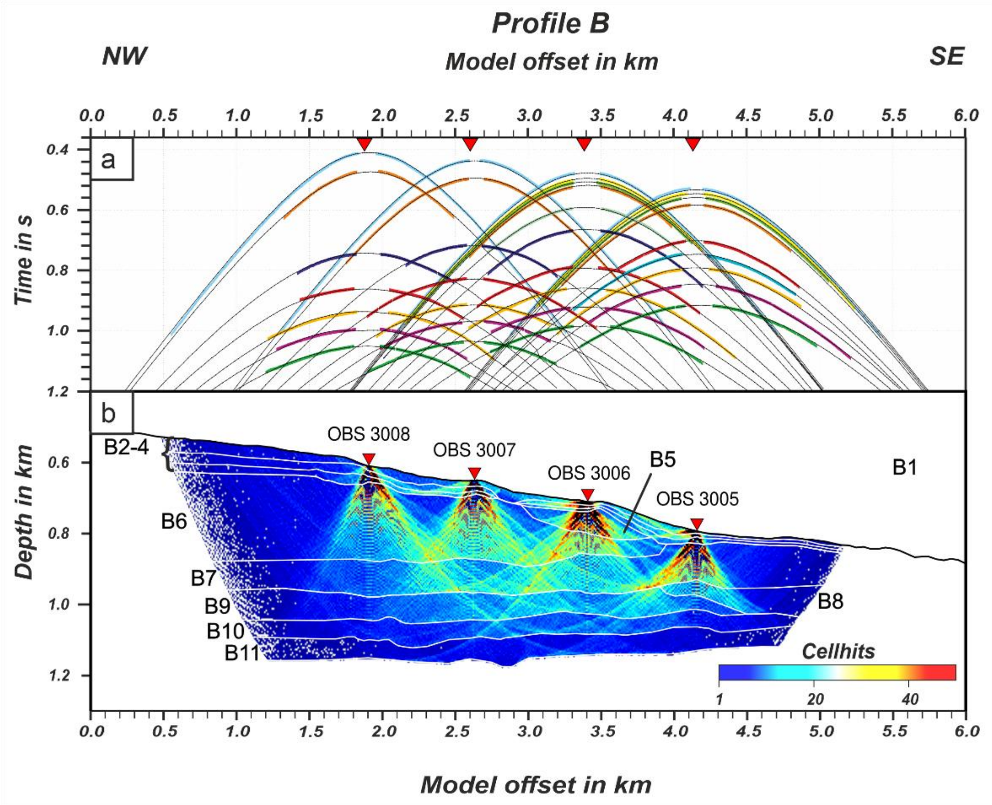

Figure S 12: Forward model assessment for the P-wave velocity model of profile B. (a) Comparison between the observed (coloured lines) and synthetic traveltime picks (black lines). (b) Ray coverage based on the ray density within the model cells.

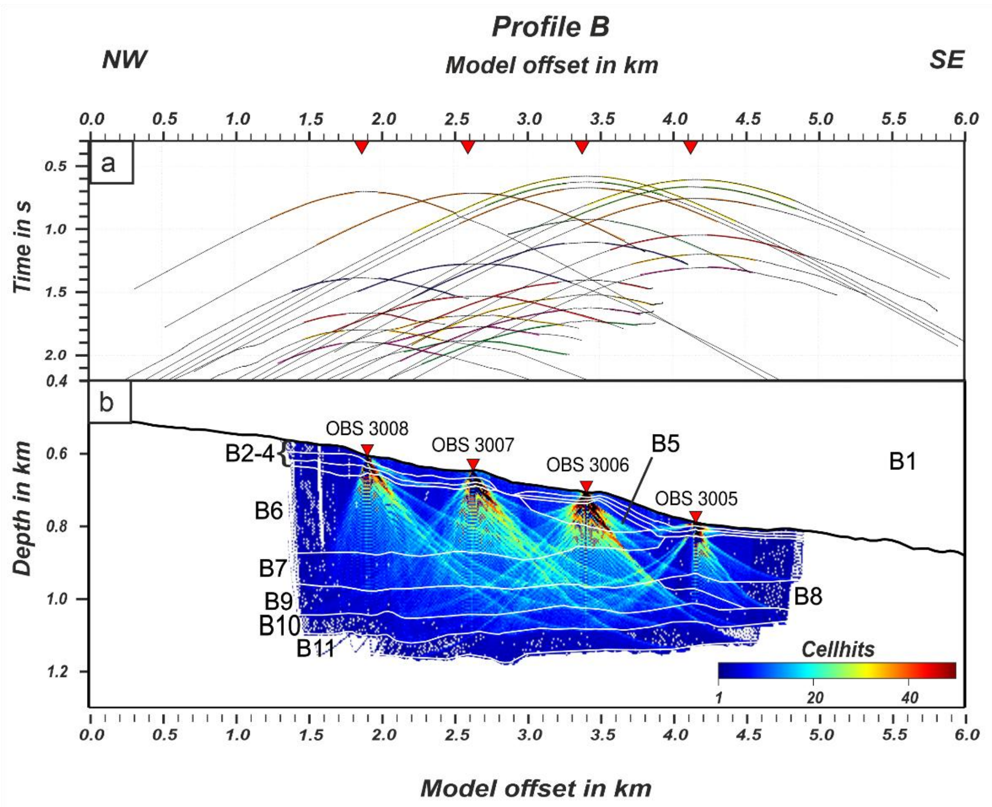

Figure S 13:Forward model assessment for the S-wave velocity model of profile B. (a) Comparison between the observed (coloured lines) and synthetic traveltime picks (black lines). (b) Ray coverage based on the ray density within the model cells.

Table S 1: *Modelled seismic velocities, Vp/Vs-ratios, and the corresponding pick uncertainties for each layer (top to bottom) for profile A.*

Layer	Vp (m/s)	Vs (m/s)	Vp/Vs-ratio	Pick uncertainty (P-/ S-wave model)	
X1	1483			5 ms / 5 ms	Water layer
X2	1510	140	10.6	5 ms / 7 ms	Unit 1
X3	1510	150	10	6 ms / -	
X4	1520	210	7.2	7 ms / 11 ms	
X5	1530	230	6.8	7 ms / 12 ms	
X6	1580-1620	320	5	7 ms / 16 ms	Unit 2
X7	1680-1720	420-430	4	10 ms / 18 ms	
X8	1640-1760	430-460	3.8	15 ms /20 ms	
X9	1760-1800	500-510	3.6	16 ms / 20 ms	Unit 3
X10	1800-1900	820-860	2.2	18 ms / 24 ms	

Table S 2: *Modelled seismic velocities, Vp/Vs-ratios, and the corresponding pick uncertainties for each layer (top to bottom) for profile B.*

Layer	Vp (m/s)	Vs (m/s)	Vp/Vs-ratio	Pick uncertainty (P-/ S-wave model)	
Y1	1483			5 ms / 5 ms	Water layer
Y2	1510	140	10.6	5 ms / 7 ms	Unit 1
Y3	1520	210	7.2	6 ms / 10 ms	
Y4	1530	230	6.8	7 ms / 12 ms	
Y5	1600-1640	280-285	5.8	10 ms / 12 ms	Unit 2
Y6	1640-1660	410-420	4	9 ms / 16 ms	
Y7	1670-1780	450-480	3.7	10 ms / 18 ms	
Y8	1800-1970	490-530	3.7	12 ms / no picks*	Unit 3
Y9	1780-1820	710-730	2.5	12 ms / 20 ms	
Y10	1820-1850	780-790	2.4	15 ms / 21 ms	
Y11	1850-1900	790-810	2.4	17 ms / 21 ms	
* Vs estimated for model continuity					

References:

Bialas, J. and Flueh, E. R.: Ocean bottom seismometers: New instrument packages demonstrates value of recording full wavefield; shows that interpretations of sediment shear wave velocities are reliable., Sea Technology, 40, 41–46, 1999.

Bialas, J., Klaucke, I., and Haeckel, M.: FS MARIA S. MERIAN Fahrtbericht / Cruise Report MSM34/1 & 2 - SUGAR Site ; Varna – Varna, 06.12.13 – 16.01.14, GEOMAR Helmholtz-Zentrum für Ozeanforschung Kiel, https://doi.org/10.3289/geomar_rep_ns_15_2014, 2014.

Diehl, T.: 3-D Seismic Velocity Models of the Alpine Crust from Local Earthquake Tomography, Dissertation, ETH Zürich, Zürich, 189 pp., 2008.

Digranes, P., Mjelde, R., Kodaira, S., Shimamura, H., Kanazawa, T., Shiobara, H., and Berg, E. W.: A regional shear-wave velocity model in the central Vøring Basin, N. Norway, using three-component Ocean Bottom Seismographs, Tectonophysics, 293, 157–174, https://doi.org/10.1016/S0040-1951(98)00093-6, 1998.

Duennebier, F. K. and Sutton, G. H.: Fidelity of ocean bottom seismic observations, Mar Geophys Res, 17, 535–555, https://doi.org/10.1007/BF01204343, 1995.

Eccles, J. D., White, R. S., and Christie, P. A. F.: Identification and inversion of converted shear waves: case studies from the European North Atlantic continental margins, Geophysical Journal International, 179, 381–400, https://doi.org/10.1111/j.1365-246X.2009.04290.x, 2009.

Essing, D., Schlindwein, V., Schmidt-Aursch, M. C., Hadziioannou, C., and Stähler, S. C.: Characteristics of Current-Induced Harmonic Tremor Signals in Ocean-Bottom Seismometer Records, Seismological Research Letters, 92, 3100–3112, https://doi.org/10.1785/0220200397, 2021.

Flinn, E. A.: Signal analysis using rectilinearity and direction of particle motion, Proc. IEEE, 53, 1874–1876, https://doi.org/10.1109/PROC.1965.4462, 1965.

Flueh, E. R. and Bialas, J.: A digital, high data capacity ocean bottom recorder for seismic investigations., 18, 18–20, 1996.

Flueh, E. R. and Grevemeyer, I.: FS Sonne Fahrtbericht / Cruise Report SO181 TIPTEQ - from The Incoming Plate to mega Thrust EarthQuakes, Valparaiso - Talcuhuano, 06.12.2004 - 26.02.2005, IFM-GEOMAR Leibniz-Institut für Meereswissenschaften an der Christian-Albrechts-Universität zu Kiel, https://doi.org/10.3289/ifm-geomar_rep_2_2005, 2005.

Hamilton, E. L.: Vp/Vs and Poisson's ratios in marine sediments and rocks, The Journal of the Acoustical Society of America, 66, 1093–1101, https://doi.org/10.1121/1.383344, 1979.

Havskov, J. and Alguacil, G.: Instrumentation in Earthquake Seismology, Springer International Publishing, Cham, https://doi.org/10.1007/978-3-319-21314-9, 2016.

Havskov, J. and Ottemoller, L.: Routine Data Processing in Earthquake Seismology, Springer Netherlands, Dordrecht, 347 pp., https://doi.org/10.1007/978-90-481-8697-6, 2010.

Jurkevics, A.: Polarization analysis of three-component array data, 78, 1725–1743, https://doi.org/10.1785/BSSA0780051725, 1988.

Maercklin, N.: Polarisationsanalyse refraktionsseismischer Daten vom Vulkan Merapi, Indonesien, Diploma Thesis, Christian-Albrechts-Universität zu Kiel, Institut for Geoscience, Geophysics (Kiel), 91 pp., 1999.

Maercklin, N.: SUPOLAR and SUPOFILT: SU programs for polarization analysis and filtering of three-component data, https://doi.org/10.13140/2.1.1697.7926, 2001.

Shearer, P. M. and Orcutt, J. A.: Surface and near-surface effects on seismic waves—theory and borehole seismometer results, Bulletin of the Seismological Society of America, 77, 1168–1196, https://doi.org/10.1785/BSSA0770041168, 1987.

Stein, S. and Wysession, M.: An introduction to seismology, earthquakes, and earth structure, Blackwell Pub, Malden, MA, 498 pp., 2003.

Stockwell, J. W.: The CWP/SU: Seismic Un∗x package, Computers & Geosciences, 25, 415–419, https://doi.org/10.1016/S0098-3004(98)00145-9, 1999.

Vidale, J. E.: Complex polarization analysis of particle motion, 76, https://doi.org/10.1785/BSSA0760051393, 1986.

Welch, P.: The use of fast Fourier transform for the estimation of power spectra: A method based on time averaging over short, modified periodograms, IEEE Trans. Audio Electroacoust., 15, 70–73, https://doi.org/10.1109/TAU.1967.1161901, 1967.

Westbrook, G. K., Chand, S., Rossi, G., Long, C., Bünz, S., Camerlenghi, A., Carcione, J. M., Dean, S., Foucher, J.-P., Flueh, E., Gei, D., Haacke, R. R., Madrussani, G., Mienert, J., Minshull, T. A., Nouzé, H., Peacock, S., Reston, T. J., Vanneste, M., and Zillmer, M.: Estimation of gas hydrate concentration from multi-component seismic data at sites on the continental margins of NW Svalbard and the Storegga region of Norway, Marine and Petroleum Geology, 25, 744–758, https://doi.org/10.1016/j.marpetgeo.2008.02.003, 2008.

Yilmaz, Ö.: Seismic Data Analysis: Processing, Inversion, and Interpretation of Seismic Data, Society of Exploration Geophysicists, https://doi.org/10.1190/1.9781560801580, 2001.